Dependence of Mass—Dimensional Relationships on Median Mass Diameter

Saisai Ding [1,2], Greg M. McFarquhar [2,3,*], Stephen W. Nesbitt [4], Randy J. Chase [4], Michael R. Poellot [5] and Hongqing Wang [1]

[1] Department of Atmospheric and Oceanic Sciences, School of Physics, Peking University, Beijing 100871, China; dingss@pku.edu.cn (S.D.); hqwang@pku.edu.cn (H.W.)

[2] Cooperative Institute of Mesoscale Meteorological Studies, Norman, OK 73072, USA

[3] School of Meteorology, University of Oklahoma, Norman, OK 73072, USA

[4] Department of Atmospheric Sciences, University of Illinois at Urbana-Champaign, Urbana, IL 61801, USA; snesbitt@illinois.edu (S.W.N.); randyjc2@illinois.edu (R.J.C.)

[5] Department Atmospheric Sciences, University of North Dakota, Grand Forks, ND 58202, USA; michael.poellot@und.edu

* Correspondence: mcfarq@ou.edu

Abstract: Retrievals of ice cloud properties require accurate estimates of ice particle mass. Empirical mass–dimensional (m–D) relationships in the form $m = aD^b$ are widely used and usually universally applied across the complete range of particle sizes. For the first time, the dependence of a and b coefficients in m–D relationships on median mass diameter (D_{mm}) is studied. Using combined cloud microphysical data collected during the Olympic Mountains Experiment and coincident observations from Airborne Precipitation Radar Third Generation, D_{mm}-dependent (a, b) coefficients are derived and represented as surfaces of equally plausible solutions determined by some tolerance in the chi-squared difference χ^2 that minimizes the difference between observed and retrieved radar reflectivity. Robust dependences of a and b on D_{mm} are shown with both parameters significantly decreasing with D_{mm}, leading to smaller effective densities for larger D_{mm} ranges. A universally applied constant m–D relationship overestimates the mass of large aggregates when D_{mm} is between 3–6 mm and temperatures are between −15–0 °C. Multiple m–D relations should be applied for different D_{mm} ranges in retrievals and simulations to account for the variability of particle sizes that are responsible for the mass and thus for the variability of particle shapes and densities.

Keywords: mass–dimensional relationship; median mass diameter; radar reflectivity; equally plausible surface

1. Introduction

Retrievals of ice cloud properties, such as radar reflectivity factor (Z) [1], snow rate [2,3], ice water content (IWC) [3,4] and effective density (ρ_e) [5,6] require estimates of how ice particle mass (m) varies with ice particle dimension (D). Accurate estimates of particle mass are thus essential to the accuracy of cloud products retrieved from remote sensing measurements [7,8]. Furthermore, microphysical parameterization schemes used in many numerical weather prediction models require accurate m–D relations to quantify microphysical processes occurring in clouds [9,10]. The m–D relations are also used to determine ice particle density, which is one of the key factors determining particle fall speeds and representing ice cloud properties in weather and numerical models. Knowledge of these relations is important because it is difficult to measure ice particle density and volume in situ because of the variability in particle shape and habit [11], and because of processes

such as aggregation, supercooled water accretion, and melting/refreezing that lead to variability in ice-air mixtures [12]. Therefore, empirical power law *m–D* relationships taking the form

$$m = aD^b \tag{1}$$

have been widely used in numerical modeling and retrieval schemes.

Various techniques and probes have been used to derive the *a* and *b* coefficients, and variations with temperature, particle habit, and cloud formation mechanism have been noted [13]. This is caused by changes in the cloud microphysical properties in different environments due to variations in the size, shape, and density of ice particles produced by the action of different microphysical processes. Previous studies deriving *a* and *b* coefficients include the following: Baran et al. [14], who determined *a* by comparing observed and calculated *Z* of cirrus, assuming an ensemble of ice aggregates and fixing *b* = 2.0; Heymsfield et al. [5,15,16], Cotton et al. [6] and Abel et al. [17] who derived *a* and *b* using measured size distributions and bulk mass contents to show variations in *b* depending on ice cloud type; and McFarquhar et al. [18] and Fontaine et al. [19] who employed ice particle images and observed bulk *Z* to derive the dependence of *b* on temperature.

Although the habit of an ice crystal is primarily a function of temperature and supersaturation [20–22], in situ observations do not show a simple correlation between particle shape, mass, temperature and humidity since many crystals are not observed in the environments in which they grow and due to imperfections in crystal shapes [23]. Nevertheless, Mitchell et al. [2] deduced *m–D* relations specific to various ice crystal habits by taking microphotographs of particles and using the melted hemispherical drops to derive *b* ranging from 1.8 (needles and long columns) to 2.6 (short columns and plates), and 2 for aggregated ice. Locatelli and Hobbs [24] also derived habit-specific *m–D* relationships for 22 particle types. Such relations can be used in combination with automatic habit classifications based on 2-D particle images [25–31] to derive *IWC* by applying specific *m–D* relations for individual habits [28,32,33] to the measured size and shape distributions. In practice, application of this technique is difficult since clouds usually consist of mixtures of complex particles, many of which have irregular shapes that cannot be unambiguously identified or represented by one of the shapes for which *m–D* relations are available. For these reasons, *m–D* relations are typically derived for mixtures of particles. Parameterizations for mixtures of particles are also easier to apply in model and remote sensing schemes.

For given conditions, the derived *a* and *b* are typically assumed to apply over the complete range of particle sizes, and hence universally applied for all particle sizes in models and retrievals. This implicitly assumes *a* and *b* are independent of particle size. However, the size dependence of *a* and *b* has been noted as Locatelli and Hobbs [24] and Mitchell [11] used different prefactors and exponents for different size ranges. Moreover, Erfani and Mitchell [34] proposed second-order polynomials for *m–D* relations that could be reduced to power laws in which the final *a* and *b* are dependent on *D*. In general, a continuous dependence of *a* and *b* on *D* is desired because the evaluation of the mass function in some cloud schemes is based on derivatives with respect to *D* and discontinuities at the overlap points produce numerical errors [35]. Furthermore, published *m–D* relations for large aggregates (i.e., *D* > 5 mm) are rare, and it remains to be seen whether these particles' masses scale as their smaller counterparts, thus potentially justifying the use of separate *m–D* relations for hydrometeor ensembles of small and large particles. This is potentially important for remote sensing retrievals of bulk hydrometeor mass in particular, where particle habits are typically not known a priori, but parameters related to number concentration and characteristic size may be retrieved in some fashion.

This paper aims to examine the dependence of *a* and *b* on a characteristic size parameter, the median mass diameter (D_{mm}), so that the retrievals of ice cloud properties can be improved. D_{mm} is defined as the *D* for which 50% of the accumulated total water content (*TWC*) is contained in smaller particle sizes and 50% in larger particle sizes, indicating the size ranges of ice particles responsible for the mass. The dependence of *m–D* relations on D_{mm} provides information for their dependence on particle size without adding a discontinuity in the relation between *D* and *m*. Here, the *a* and *b* are derived following the approach of Finlon et al. [13] using in situ microphysical and coincident remote sensing data collected during the 2015 Olympic Mountains Experiment (OLYMPEX) conducted in

and offshore of western Washington State [36]. The remainder of the manuscript is organized as follows. Section 2 describes methods used to process in situ and coincident remote sensing data from OLYMPEX, and to derive microphysical variables and m–D relations dependent on D_{mm}. The dependence of m–D relations on D_{mm} is quantified and discussed in Section 3. The key results are summarized in Section 4.

2. Data and Methods

2.1. OLYMPEX Measurements

During OLYMPEX, the University of North Dakota Cessna Citation II (N55DS) [37] flew 20 missions, collecting in-cloud measurements at temperatures between −60 °C and 12 °C. Optical Array Probes (OAPs) that obtain particle images from the occultation of a laser beam incident upon an array of fast response photodiodes included a 2D Stereo Probe (2D-S), nominally sizing particles from 10 to 1280 μm, and a Version 3 High Volume Precipitation Spectrometer (HVPS-3), sizing particles from 150 to 19,200 μm. Data from the OAPs were processed with the University of Illinois/Oklahoma Optical Array Probe Processing Software (UIOOPS) using particle inter-arrival times to remove shattered artifacts from the 2D-S data using algorithms introduced by [38,39]. Particle size distributions (PSDs) for the maximum dimension 200–30,000 μm were determined by merging the 2D-S vertical array with the vertically oriented HVPS-3 with a crossover between probes at 1000 μm. Particles larger than the diode array were reconstructed following the method in [40] provided their center was determined to be within the photodiode array.

To provide radar data that gives the larger scale context of the microphysics observations and give data coincident with in situ microphysics observations, the National Aeronautics and Space Administration (NASA) DC-8 aircraft carrying the Airborne Precipitation Radar Third Generation (APR-3), a triple-frequency (Ku-, Ka-, and W-bands, 13, 35, and 94 GHz respectively) Doppler, dual-polarization radar system [41,42], flew flights at mostly constant altitude above the Citation during OLYMPEX. Radar volumes collected within 10 min temporally and 1 km spatially of the Citation are regarded as collocated following Chase et al. [43]. More details about the specifics of collocation and calibration of the radar measurements are found in [43].

In this study, the lower bound for the PSD is set at 200 μm to exclude any possible contributions from supercooled drizzle drops whose maximum sizes were around 200 μm during OLYMPEX [43]. PSDs are averaged every 5 s and analysis is restricted to periods when the total number concentration of particles with $D > 200$ μm was greater than 10^3 m^{-3} to ensure that the Citation was within more than just a tenuous cloud. To restrict the analysis to ice-phase clouds, only periods with total number concentrations measured by the Cloud Droplet Probe (CDP) [44] less than 10 cm^{-3} are used following [45]. There are 5928 5-s observations (8.23 h in total) in ice clouds with coincident radar observations at temperatures between −33 °C and −1 °C. For ice-phase clouds, the *TWC* is equivalent to the *IWC*.

2.2. Derivation of Bulk Properties

Several bulk quantities can be calculated from the PSD when an m–D relation is assumed. First, the *IWC* can be derived following

$$IWC = \sum_{D_{min}}^{D_{max}} m\, N(D)\, \Delta D, \tag{2}$$

where $N(D)$ is the ice particle number distribution function for the size bin with midpoint D, and m is crystal mass determined from Equation (1) and restricted to be less than the mass of an ice spheroid of the same D with aspect ratio 0.6 following the approach of Hogan et al. [46]. For ice-phase clouds, D_{mm} is determined as

$$\frac{1}{2} IWC = \sum_{D_{min}}^{D_{mm}} m\, N(D)\, \Delta D = \sum_{D_{mm}}^{D_{max}} m\, N(D)\, \Delta D. \tag{3}$$

The D_{mm} derived from Equation (3) is mainly a function of b [47]. Initially, D_{mm} is calculated using a prior m–D relation $m = 0.0061D^{2.05}$ from a study of Heymsfield et al. in 2004 ([5], hereafter HY04) and subsequently referred to as $D_{mm,hy}$. The HY04 coefficients a and b originally introduced are specific to ice crystals generated in synoptically and convectively generated ice clouds, which have been widely used in model parameterization schemes. Previous study has shown that the HY04 m–D relationship gives reasonable estimates of reflectivity at Ku-band for temperatures below 0 °C during OLYMPEX [48]. Here, $D_{mm,hy}$ is used as a descriptor of PSDs and for comparisons with results generated from new (a, b) parameters. Sensitivity studies conducted here using other m–D relations (e.g., [4]) showed that similar conclusions were reached regardless of what m–D was used to calculate the initial values of D_{mm} (figures not shown).

The effective density of the ice particle population (ρ_e) for each 5-s PSD is calculated by

$$\rho_e = \frac{TWC}{V},$$ (4)

and

$$V = \sum_{D_{min}}^{D_{max}} 0.6 \times \frac{\pi}{6} D^3 N(D) \Delta D,$$ (5)

where V is the total volume of all ice particles assuming they are spheroids with diameter D and aspect ratio 0.6. ρ_e describes the density of a collection of ice particles rather than of single ice particles.

For all D corresponding to the center of the size bins and for given a and b coefficients, the radar reflectivity factor at the Ku-band is forward modeled using the Rayleigh–Gans spheroid approximation that was described in detail by Hogan et al. [46] and integration of backscatter cross-section over the PSD yields total reflectivity. The Rayleigh–Gans theory was first introduced by van de Hulst [49], and modifies the Rayleigh scattering law to incorporate the interference of out-of-phase scattered waves of the scatterer. It has been found that the Rayleigh–Gans spheroid approximation performs well for modeling the scattering properties of aggregates in ice clouds for particle sizes no larger than the wavelength considered [46]. Other scatter models including the Rayleigh theory and a Self-Similar Rayleigh–Gans theory [50], are also examined here and further discussed in Section 3. The Ku-band is used because it experiences less attenuation and fewer non-Rayleigh scattering effects than other bands of reflectivity collected during OLYMPEX (Ka and W band), and thus these scattering models should perform well in this scattering regime. The systematic errors of Rayleigh–Gans approximation are reported to be very small at Ku-band for unrimed snowflakes with mean bias of at most 1dBZ [51,52].

As stated in Section 2.1, particles smaller than 200 μm are removed to eliminate any possible influence of supercooled liquid droplets in the measured $N(D)$. To assess the contribution of small particles to derived properties, using the same HY04 m–D relation, the ratios of D_{mm}, IWC and equivalent radar reflectivity factor Z derived from PSDs with minimum sizes of 125 μm and 200 μm were calculated. The average ratios $D_{mm,PSD>200}/D_{mm,PSD>125}$, $IWC_{PSD>200}/IWC_{PSD>125}$, $Z_{PSD>200}/Z_{PSD>125}$ are 1.03, 0.98, and 0.99 respectively, showing small particles with 125 μm < D < 200 μm, where there are the larger uncertainties in the measured PSDs [53], contribute less than 5% to those derived quantities. Reliable PSD observations for ice particles with D < 125 μm are not available during OLYMPEX, but their contributions to mass and reflectivity are expected to be minimal [53].

2.3. Constraint of m–D Relationships

The estimates of (a, b) parameters consistent with the measured bulk properties can be determined by minimizing the chi-squared differences (χ^2) between quantities derived from size distributions and bulk measured values. In particular, the χ^2 metric defining the difference between Ku-band Z derived from $N(D)$ ($Z_{Ku,psd}$) and those directly measured by the Ku-band APR-3 (Z_{Ku}), is given by

$$\chi^2(a, b) = \frac{1}{n} \sum \frac{\left(Z_{Ku,psd} - Z_{Ku}\right)^2}{Z_{Ku,psd} \times Z_{Ku}}, \tag{6}$$

where *n* is the number of samples. The definition of χ^2 in Equation (6) follows Finlon et al. [13]. The bulk measured *TWC* by Nevzorov probe could also be used to calculate χ^2 taking into account differences between both derived and observed *Z* and *TWC* [13], where *TWC* is equal to *IWC* for ice-phase clouds. However, the Nevzorov probe has been found to underestimate the *TWC* in previous studies due to the potential problem of ice crystals bouncing out from its sensor especially for particles larger than 4 mm [54,55], and thus is not used in this study.

In the calculation of χ^2, Equation (1) is slightly modified to the form

$$m = a \left(\frac{D}{D_0}\right)^b, \tag{7}$$

where $D_0 = 1$ cm, so that *b* is dimensionless and *a* has a single physical dimension of mass, such as grams, rather than having its units depending on *b*. Equation (7) solves the potential problem of comparing incommensurable quantities *a* in g cm^{-b} with varying values of *b*. The χ^2 is computed for all *a* and *b* for $2.00 \times 10^{-4} < a < 0.05$ g and $1.00 < b < 5.00$ with increments of 2.00×10^{-4} g for *a* and 0.02 for *b* in order to find the minimum χ^2 (hereafter χ^2_{min}) and thus most likely *a* and *b*. It is assumed that all *a* and *b* that have $\chi^2 < \chi^2_{min} + \Delta\chi^2$ are equally plausible solutions, where $\Delta\chi^2$ defines the allowed tolerance. The choice of $\Delta\chi^2$ is discussed in Section 3.

3. Results

3.1. Dependence of (a, b) on D_{mm}

3.1. Dependence of (a, b) on D_{mm}

3.1.1. Behavior of Equally Plausible Surfaces

The 5-s time averaged PSDs are sorted into different populations according to $D_{mm,hy}$. For each population, χ^2 is calculated using Equation (6) by summing over PSDs in the appropriate population. One population includes all PSDs with $200 \le D_{mm,hy} < 500$ μm whereas the other 11 populations correspond to $D_{mm,hy}$ equally spaced between 500 and 6000 μm. PSDs with $D_{mm,hy}$ larger than 6000 μm were excluded from the analysis because there were only 37 (0.62% of the total) such PSDs which was not regarded as statistically significant. The (*a*, *b*) minimizing χ^2 was hence determined for each population.

Different uncertainty sources are considered to define the tolerance of the minimum χ^2 for each population. When conducting fits to observed PSDs, McFarquhar et al. [56] defined $\Delta\chi^2 = \max(\Delta\chi_1^2, \chi^2_{min})$, where $\Delta\chi_1^2$ represented uncertainties in the observed PSDs due to statistical sampling uncertainties and χ^2_{min} characterized the robustness of the minimization procedure related to how well the observed PSD fit the assumed gamma distribution and how much variability there was in the size distributions. Here, this technique was followed and $\Delta\chi_1^2$ for each $D_{mm,hy}$ bin is defined using the statistical uncertainty in the sampled PSD as

$$\Delta\chi_1^2\left(D_{mm,hy}\right) = \frac{1}{2n} \sum \left[\frac{\left(Z_{Ku,psd,max} - Z_{Ku,psd}\right)^2}{Z_{Ku,psd,max} \times Z_{Ku,psd}} + \frac{\left(Z_{Ku,psd,min} - Z_{Ku,psd}\right)^2}{Z_{Ku,psd,min} \times Z_{Ku,psd}} \right], \tag{8}$$

where $Z_{Ku,psd}$ are calculated using the most likely (*a*, *b*) that minimizes χ^2, $Z_{Ku,psd,max}$ and $Z_{Ku,psd,min}$ are the maximum and minimum *Z* derived using the maximum and minimum *N(D)* using the same *m*–*D* relation. The maximum and minimum *N(D)* are determined by adding and subtracting the square root of the number concentration in each size bin corresponding to adding or subtracting square root of the number of counts in that bin [56,57] as the square root of the number of counts gives a measure of the statistical uncertainty based on Poisson Statistics.

Uncertainties associated with the observed *N(D)* by OAPs and Ku-band *Z* by APR-3, are also considered using $\Delta\chi_2^2$, which is defined as

$$\Delta\chi_2{}^2\left(D_{mm,hy}\right)$$

$$= \frac{1}{2n}\sum\left\{\begin{matrix}\left[\dfrac{\left(\sqrt{Z_{Ku,psd,max2}}-\sqrt{Z_{Ku,psd}}\right)^2}{\sqrt{Z_{Ku,psd,max2}}\times\sqrt{Z_{Ku,psd}}}+\dfrac{\left(\sqrt{Z_{Ku,meas,max}}-\sqrt{Z_{Ku}}\right)^2}{\sqrt{Z_{Ku,meas,max}}\times\sqrt{Z_{Ku,psd}}}\right]+\\[2mm]\left[\dfrac{\left(\sqrt{Z_{Ku,psd,min2}}-\sqrt{Z_{Ku,psd}}\right)^2}{\sqrt{Z_{Ku,psd,min2}}\times\sqrt{Z_{Ku,psd}}}+\dfrac{\left(\sqrt{Z_{Ku,meas,min}}-\sqrt{Z_{Ku,psd}}\right)^2}{\sqrt{Z_{Ku,meas,min}}\times\sqrt{Z_{Ku,psd}}}\right]\end{matrix}\right\}, \tag{9}$$

where $Z_{Ku,psd,max2}$ and $Z_{Ku,psd,min2}$ are the maximum and minimum Z derived assuming that the $N(D)$ measured by the OAPs has 50% uncertainties [58]. The $Z_{Ku,meas,max}$ and $Z_{Ku,meas,min}$ represent the maximum and minimum measured Z derived by the uncertainties of measured Z_{Ku} during OLYMPEX of 1 dB following Chase et al. [43].

Uncertainties from different sources are compared in Figure 1a. It is found that $\Delta\chi_1{}^2/\chi^2{}_{min} < 10^{-3}$ for all 12 populations, which means the robustness of the minimization procedure is a greater uncertainty than the statistical uncertainty associated with the PSD sampling. The $\Delta\chi_2{}^2/\chi^2{}_{min}$ ranged between 0.16 and 0.64 with a mean value of 0.34, suggesting that observation uncertainties are comparable with the robustness of the minimization procedure, but it is still the minimization procedure that mainly dominates in the variability of the relationship.

Equally plausible surfaces for each population colored by $D_{mm,hy}$ using the tolerance $\chi^2{}_{min}$ and $\Delta\chi_2{}^2$ are shown in Figure 1b,c respectively. As $\chi^2{}_{min}$ is greater than $\Delta\chi_2{}^2$ for each population, the areas of surfaces determined by $\chi^2{}_{min}$ are larger than those determined by $\Delta\chi_2{}^2$. However, all surfaces have narrow spheroid-like shapes in the parameter space with their locations offset from each other as a function of $D_{mm,hy}$. As $D_{mm,hy}$ increases, the surfaces tend to rotate clockwise with the orientation of surfaces getting more horizontal and more prolate, indicating a smaller range of allowable values of *a* and larger variations of *b* for larger $D_{mm,hy}$.

The same clockwise shift of the equally plausible surfaces with increasing $D_{mm,hy}$ is present when the tolerance of surfaces differs, showing the dependence of how the surfaces varied with $D_{mm,hy}$ is robust. However, the exact range and location of the surfaces depend on the methodology and threshold used to generate the surfaces. For example, the surfaces can even extend beyond the sample ranges of *a* and *b* for $D_{mm,hy} < 500$ μm and $D_{mm,hy} > 4500$ μm especially (Figure 1b).
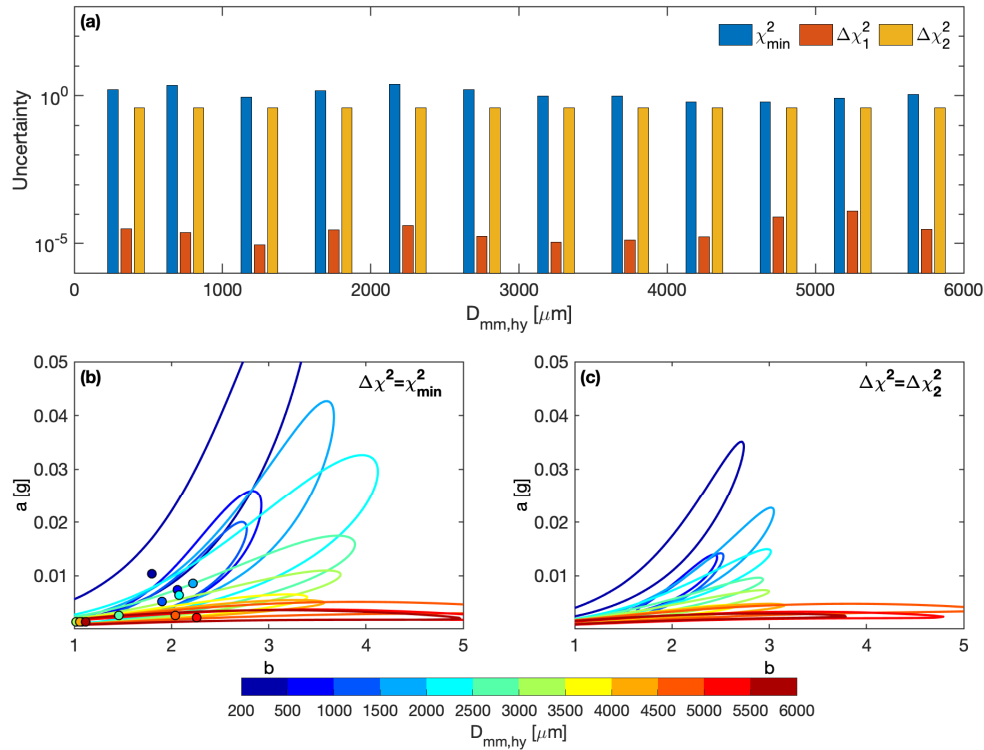
Figure 1. (**a**) Sources of uncertainties as a function of $D_{mm,hy}$; (**b**) Equally plausible surfaces determined by $\chi^2 = 2\chi^2_{min}$ for different $D_{mm,hy}$ range bins indicated by the color bar beneath the plot. Circles with corresponding colors denote the locations of χ^2_{min} for each $D_{mm,hy}$ bin. (**c**) Same as (**b**) but equally plausible surfaces determined by $\chi^2 = \chi^2_{min} + \Delta\chi_2^2$.

3.1.2. Quantitative Dependences of (a, b) and ρ_e on D_{mm}

To further demonstrate the dependence of a and b on $D_{mm,hy}$, 300 (a, b) solutions are randomly chosen from each of the equally plausible surfaces in Figure 1b. These solutions are used to examine the physical realism of the solutions, and for examining the dependence of a, b and ρ_e on D_{mm}.

The equally plausible surfaces in Figure 1 are showing that b coefficients could be greater than 3, which may seem physically impossible as the mass of a particle cannot be greater than that of an ice sphere with the same D. However, due to the covariability of a and b, $b > 3$ does not necessarily imply the particle has a mass greater than a sphere. Instead, it merely indicates how the mass (and hence density) varies as a function of D. In the absence of any additional information (e.g., role of fractal dimension in determining the value of b), minimizing the difference between bulk measured quantities and those obtained by integrating PSDs does not constrain values of b to be less than 3. Furthermore, Abel et al. [17] previously used b values greater than 3 to calculate the *IWC* from size distributions where highly rimed particles dominated. It is verified that all random (a, b) solutions within the equally plausible surfaces in Figure 1, including those with $b > 3$, generate smaller mass of single particle than that of an ice sphere with the same maximum dimension D. It means that these solutions represent physically realistic values. However, if b were greater than 3, the density of particles would necessarily increase with maximum dimension, which has not been commonly observed. Given that no consensus has been reached on the possibility of $b > 3$ and because physical arguments mean such values are likely unrealistic, $b > 3$ solutions are excluded in subsequent analysis.

The mean and quartiles of the a and b randomly selected from the surfaces are shown in Figure 2a and 2b as a function of $D_{mm,hy}$. As $D_{mm,hy}$ gets larger, a prominently decreases with $D_{mm,hy}$, especially for $D_{mm,hy} > 2000$ µm. This is consistent with the clockwise rotating surfaces with $D_{mm,hy}$ in Figure 1b.

Significant linear correlation is found between the mean values of *a* solutions and $D_{mm,hy}$ with correlation coefficient equal to −0.83. The large mean values and spreads of *a* over $D_{mm,hy} < 500$ μm and $D_{mm,hy}$ between 1500–2500 μm are caused by the larger surfaces for these $D_{mm,hy}$ range, where the uncertainties from minimizing procedures (χ^2_{min}) are larger than other $D_{mm,hy}$ ranges. Clear decreasing variation of *b* with $D_{mm,hy}$ is also denoted by a negative slope (−0.04 mm^{-1}) between the mean values of random *b* solutions and $D_{mm,hy}$, which is significant at the 95% confidence level. Compared to the HY04 *m–D* relation coefficients, for $D_{mm,hy} < 3000$ μm, most of the *a* (75.7%) and *b* (70.4%) solutions are greater than those of HY04, but for $D_{mm,hy}$ between 3–6 mm, most of *a* (95.6%) and near half of *b* (41.8%) get lower values than HY04.
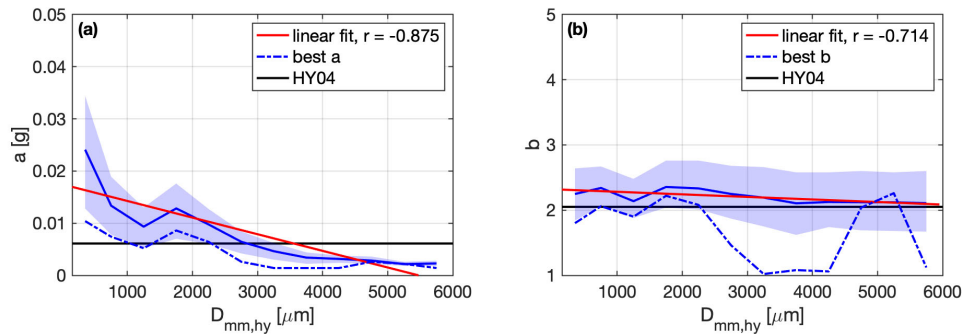
Figure 2. (**a**) Equally plausible solutions of *a* and (**b**) *b* determined by the equally plausible surfaces in Figure 1b. The blue solid lines, lower bounds and upper bounds of the blue shading areas represent mean values, 25% and 75% percentiles of *a* and *b* solutions respectively in each $D_{mm,hy}$ bins. Blue dashed lines indicate the beat estimate of (*a*, *b*) that minimizes χ^2 in each $D_{mm,hy}$ bins. Red lines show the linear regression lines of mean values with linear correlation coefficients r shown in legends. Black lines indicate the *a* and *b* coefficients of HY04 *m–D* relationship.

The best estimates of (*a*, *b*) pairs that minimize the χ^2 in each $D_{mm,hy}$ bin generally exhibit similar trends to the statistics of random selected solutions. However, these best *a* and *b* estimations are almost all smaller than the first quartiles of random solutions in their corresponding $D_{mm,hy}$ ranges. For $D_{mm,hy} < 2500$ μm, the best *a* and *b* fluctuate around the HY04 *m–D* values, indicating that the HY04 *m–D* relationship performs well for most ice clouds during OLYMPEX with $D_{mm,hy} < 2500$ μm (81.3%). For 19.4% of the total periods with $D_{mm,hy} > 2500$ μm, except *b* = 2.04 for $D_{mm,hy}$ between 4500–5000 μm and *b* = 2.26 for $D_{mm,hy}$ between 5500–5000 μm, best estimations of *a* and *b* are notably smaller than the *a* and *b* in the HY04 *m–D* relation. This implies that the HY04 *m–D* relationship conceivably overestimates particle mass when $D_{mm,hy}$ is greater than 3 mm.

Knowledge of the ice effective density (ρ_e) can also be informative. As shown in Figure 3, different *m–D* relationships produce consistently decreasing ρ_e with increasing $D_{mm,hy}$. For $D_{mm,hy} < 500$ μm, although the ρ_e derived from the HY04 *m–D* relationship (henceforth ρ_{e0}) are lower than ρ_e derived from randomly selected (*a*, *b*) solutions in Figure 2 (henceforth ρ_{e1}), there is no significant differences between ρ_{e0} and ρ_{e1} as ρ_{e1} is highly variable as a function of $D_{mm,hy}$. For $D_{mm,hy} > 1500$ μm, ρ_{e0} is significantly greater than ρ_{e1} with a mean difference of 2.21 ± 0.89 g cm^{-3}. The ρ_{e0} and ρ_{e1} tend to converge at $D_{mm,hy}$ around 4500 μm to 0.03 g cm^{-3} and 0.01 g cm^{-3}, respectively.
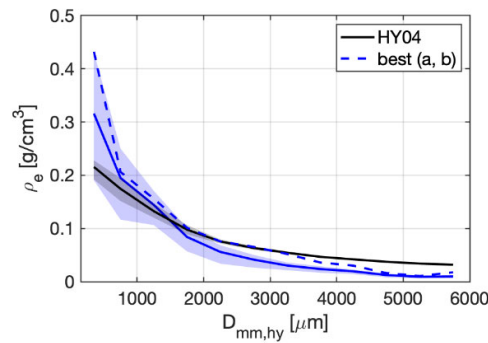
Figure 3. Effective density (ρ_e) determined by different *m–D* relations. The blue solid line, lower bound and upper bound of the blue shading areas represent mean values, 25% and 75% percentiles of ρ_e respectively. Blue dashed line indicates the ρ_e derived from the best estimate of (*a*, *b*) that minimizes χ^2 in each $D_{mm,hy}$ bins. Black line denotes ρ_e derived from the HY04 *m–D* relationship.

3.2. Implications for $D_{mm,hy}$ between 3–6 mm

By minimizing the χ^2 of Ku-band radar reflectivity between APR-3 observations (Z_{Ku}) and those derived from PSDs ($Z_{Ku,psd}$), the dependence of *m–D* relation coefficients on $D_{mm,hy}$ was demonstrated in Section 3.1. The best estimates of *a* and *b* coefficients differ from the HY04 coefficients especially when $D_{mm,hy}$ is greater than 3 mm (Figure 2). This is also revealed by the comparisons between Z_{Ku} and $Z_{Ku,psd}$ using the HY04 (Figure 4a) coefficients and the $D_{mm,hy}$-dependent *m–D* relationships (Figure 4b). The HY04 *m–D* relation provides accurate estimates of radar reflectivity for $D_{mm,hy}$ < 3000 μm, with a median ratio of $Z_{Ku,psd}/Z_{Ku}$ (hereafter R_z) 1.01 and a mean ratio of 1.52 ± 2.75, which means an average bias of 0.34 ± 4.37 dB; For $D_{mm,hy}$ > 3000 μm, R_z tends to increase with $D_{mm,hy}$, with median values rising from 1.80 to 9.81 and mean values rising from 2.15 to 12.87, indicating average overestimates of $Z_{Ku,psd}$ of 4.00–11.10dB. Using the $D_{mm,hy}$-dependent *m–D* relationships derived from the best estimates of *a* and *b* that minimized the χ^2 in each population of PSDs, the overestimated $Z_{ku,psd}$ for $D_{mm,hy}$ > 3000 μm are much improved with a median R_z of 0.90 and mean R_z of 1.42 ± 1.92 (Figure 4b).

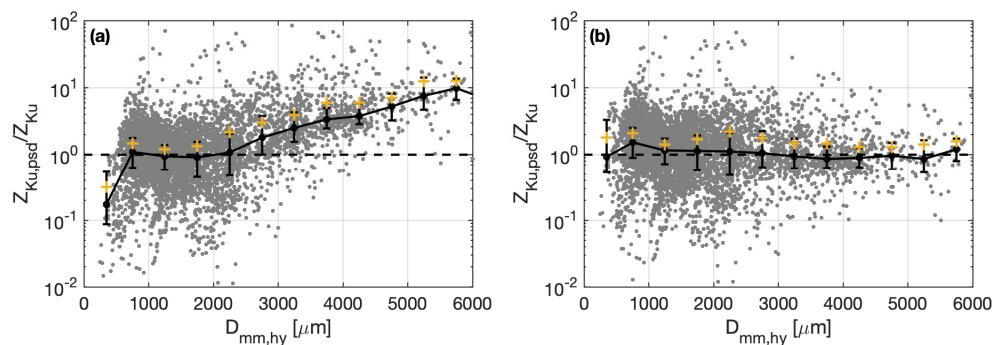**Figure 4.** Ratios of radar reflectivity derived from PSD ($Z_{Ku,psd}$) to the bulk measured Ku-band reflectivity (Z_{Ku}) using (**a**) HY04 *m–D* relation and (**b**) best estimate of (*a*, *b*) that minimizes χ^2 in each $D_{mm,hy}$ bins. The black solid lines and error bars represent median values, 25% and 75% percentiles of $Z_{Ku,psd}/Z_{Ku}$ in each $D_{mm,hy}$ bins. Yellow plus signs are the mean values for each $D_{mm,hy}$ bins. Black dashed lines denote the 1:1 line.

Various scattering models including the Rayleigh–Gans spheroid approximation, Rayleigh, and the Self-Similar Rayleigh–Gans approximation are examined to evaluate the uncertainties of the

derived $Z_{Ku,psd}$. Using the same HY04 *m–D* relationship, the overall average ratios of *Z* based on the Rayleigh–Gans spheroid approximation to the *Z* based on Rayleigh approximation and the *Z* based on the Self-Similar Rayleigh–Gans approximation are 0.92 and 1.00 respectively with differences between them less than 0.1 dB; Restricted to $D_{mm,hy}$ between 3–6 mm, these ratios are 0.80 and 0.93. The ratios of R_z exhibit undistinguishable trends with $D_{mm,hy}$ as shown in Figure 4a regardless of the scatter scheme. The discrete dipole approximation [59], which is commonly used as the reference method of choice for snowflake scattering calculations [60,61], is not examined given the limitation of computation resources. However, given recent studies by Leinonen et al. [52], the average scattering properties given by the Rayleigh–Gans approximation are in good agreement with the discrete dipole approximation for all but the most heavily rimed snowflakes, with the mean bias in the backscattering cross-section no more than 1 dB. Therefore, uncertainties brought by the scattering scheme do not affect the fact that HY04 *m–D* relation overestimates *Z* for $D_{mm} > 3$ mm in ice only clouds.

The characteristics of clouds with large $D_{mm,hy}$ are shown in Figure 5. The number of particles smaller or greater than 3 mm in the PSDs varies considerably depending upon $D_{mm,hy}$. The number of particles greater than 3 mm tends to increase sharply with $D_{mm,hy}$ and the number of those smaller than 3 mm decreases with $D_{mm,hy}$. This confirms that $D_{mm,hy}$ gives information about the shapes of PSDs and shows the size ranges responsible for mass. Dependence of *a* and *b* on $D_{mm,hy}$ also implies dependence on particle size dimension *D*. Clouds with $D_{mm,hy}$ between 3 and 6 mm were mainly observed when temperatures ranged between −15–0 °C during OLYMPEX, of which 65.7% were between −15–−10 °C and 27.7% were between −10–−5 °C (Figure 5b). Examples of typical particle images for large $D_{mm,hy}$ periods are shown in Figure 5c: aggregates of dendrites with sizes between 3 and 5 mm and even snowflakes near 1 cm are evident. These dominant secondary habits clearly illustrate that aggregation is a dominant growth mechanism for these particles.
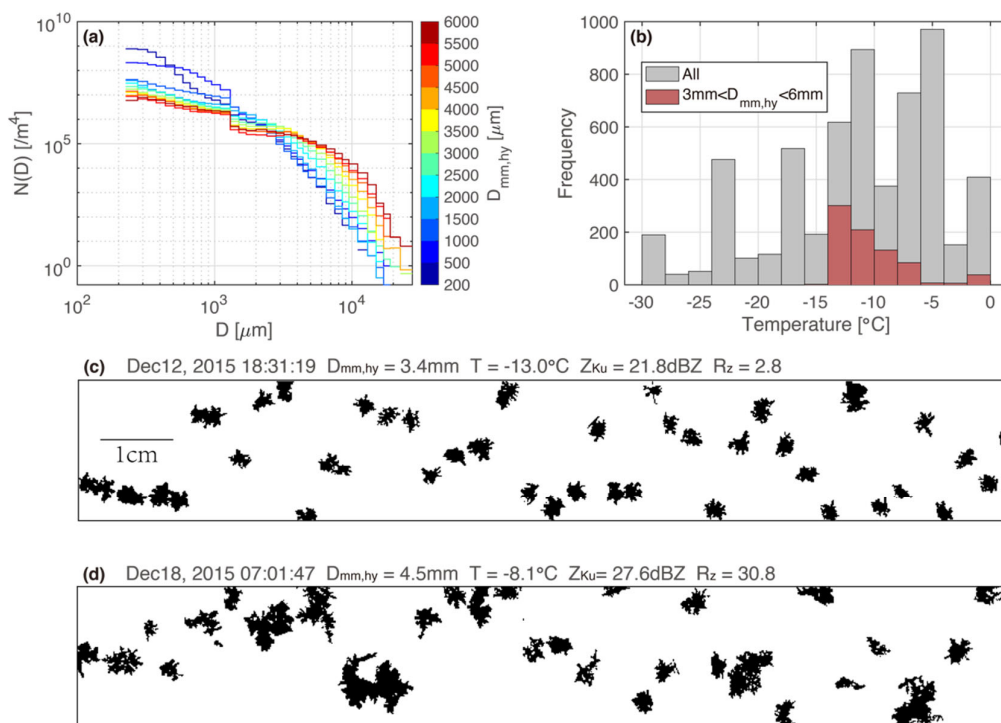

Figure 5. (**a**) Averaged PSDs for different $D_{mm,hy}$ ranges indicated by the color bar; (**b**) Histograms of temperature for all ice clouds (gray) and $D_{mm,hy}$ between 3–6 mm (red); (**c,d**) typical particle images from HVPS probe for $D_{mm,hy}$ between 3–6 mm.

Previous studies have rarely focused on establishing an *m–D* relation for particles with *D* greater than 3 mm or periods when median mass dimensions D_{mm} are greater than 3 mm. Mitchell [3] suggests two *m–D* relationships for aggregates of side planes between 600–4100 μm and for aggregates of side planes, columns, and bullets between 800–4500 μm respectively; Leroy et al. [62] analyzed the size characteristics of tropical storm clouds with D_{mm} ranging between 250 and 800 μm and peaking up to 2 mm, in which the vapor deposition contributes the major growth of ice particles. Therefore *m–D* relations for natural conditions where single pristine shapes are not present and where particles with dimensions larger than 3 mm are present have not been discussed before, making the relations presented here unique.

However, many different *m–D* relationships for aggregates have been reported based on field measurements: Schmitt and Heymsfield [63] give *a* = 0.0068, *b* = 2.22 for aggregates, which are both greater than the *a* and *b* of HY04 and will overestimate *IWC* and *Z* compared with the results of this study; Locatelli and Hobbs [24] give *a* = 0.0037, *b* = 1.9 for rimed aggregates of dendrites; Mitchell [3] reports *a* = 0.033, *b* = 2.22 for aggregates of side planes and *a* = 0.028, *b* = 2.1 for aggregates of side planes, columns, and bullets; Tyynelä et al. [60] obtain *a* = 0.0036, *b* = 1.57 for the fernlike aggregates. Single particle masses derived from these *m–D* relations are plotted in Figure 6 and compared with the mass derived from the best estimates of *a* and *b* shown in Figure 2. All four of the *m–D* relations reported for the different kinds of aggregates in Figure 6 produce smaller particle masses for particles with *D* greater than 3 mm compared to HY04 (black dashed line). Furthermore, they produce smaller *m* for *D* greater than 3 mm compared to the $D_{mm,hy}$-dependent *m–D* relations derived for $D_{mm,hy}$ < 2500 μm, but larger *m* than that using the *m–D* relations derived for $D_{mm,hy}$ > 3 mm. Given that the HY04 *m–D* relationship predicts particle masses larger than the other relationships when large aggregates greater than 3 mm are abundant, it or any other constant *m–D* relationships is likely not appropriate for use under such conditions.
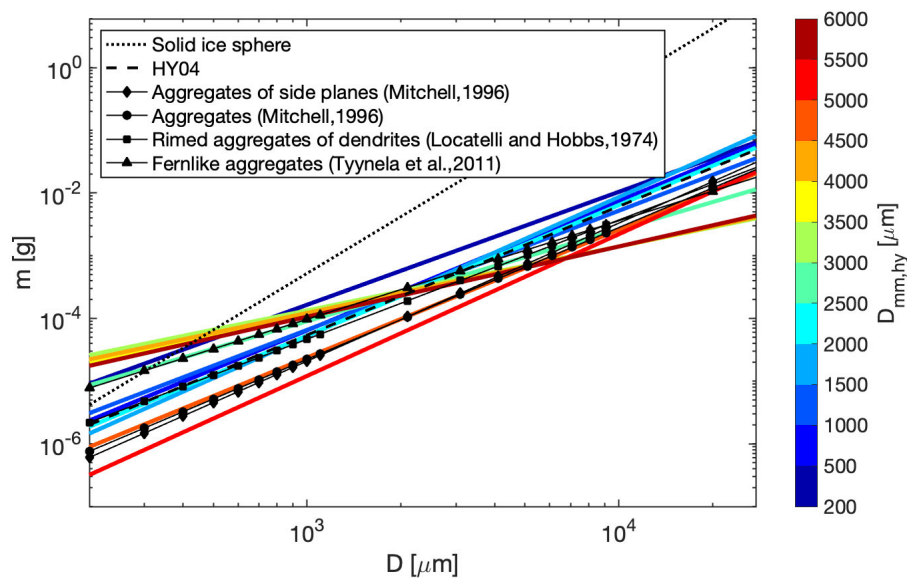

Figure 6. Single particle mass derived from different *m–D* relations. Colored solid lines are the single particle masses derived from the best estimates of (*a*, *b*) in Figure 2 for different $D_{mm,hy}$ ranges indicated by the color bar.

The $D_{mm,hy}$ has been used here as a surrogate for the actual value of median mass dimension D_{mm}. The actual D_{mm} is dependent on the *a* and especially the *b* coefficient derived; the dependence of *a* and *b* on this D_{mm} could thus be derived with an iterative approach. Figure 7 shows the relationship between $D_{mm,hy}$ and D_{mm}. The D_{mm} derived from random selected solutions within equally plausible surfaces (Figure 2) are well correlated with $D_{mm,hy}$ with a correlation coefficient 0.91 and mean difference 137.53 ± 455.30 μm. For the best estimates of (*a*, *b*), although the mean D_{mm} is 1.1 mm smaller

than $D_{mm,hy}$ for $D_{mm,hy}$ between 3–4.5 mm, there is still a significant linear correlation between D_{mm} and $D_{mm,hy}$ for all $D_{mm,hy}$ ranges with a correlation coefficient 0.89. The sharp decrease of the best estimate of b between 3 and 4.5 mm seen in Figure 2 is responsible for the D_{mm} being smaller than $D_{mm,hy}$ in this size range. As shown in Figure 1b, for $D_{mm,hy}$ between 3 and 4.5 mm, the position of the minimum χ^2 is near the lower left, meaning the best a and b that minimize χ^2 are both very small. These low values of a, b and D_{mm} show why a single best estimate of (a, b) for characterizing the m–D relation is inadequate: although the best estimate of a and b between 3 and 4.5 mm are inconsistent with values in other size ranges, the (a, b) surface is consistent with the other surfaces showing the need for a statistical approach.
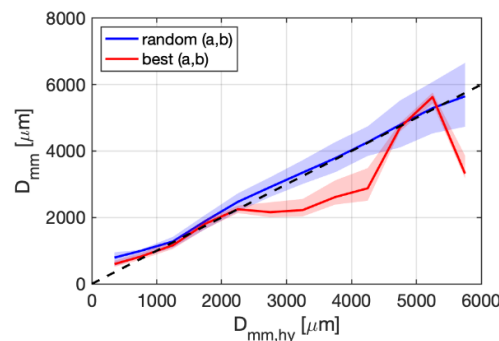

Figure 7. The D_{mm} derived by $D_{mm,hy}$-dependent m–D relationship compared to the $D_{mm,hy}$. The blue and red solid line represent the mean D_{mm} derived from random equally plausible (a, b) solutions and the best estimate of (a, b) that minimizes χ^2 in each $D_{mm,hy}$ bins respectively. The lower and upper bounds of shading areas with corresponding colors indicate the 25% and 75% percentiles of D_{mm} in each $D_{mm,hy}$ bins.

Thus, it is seen that the dependence of a and b on $D_{mm,hy}$ derived in this study is well representative of how they vary with $D_{mm,hy}$. Therefore, $D_{mm,hy}$ in this paper is regarded as an index describing the ice particle size ranges responsible for masses. With the difficulties to identify every particle's habit in retrievals and simulations, D_{mm} is thus a better descriptor than temperature for constraining m–D relationships. D_{mm} has its unique advantage in identifying periods when large aggregated particles with maximum dimensions greater than 3 mm dominate. Multiple m–D relations should be applied for different D_{mm} ranges so that the masses of large and less dense particles such as aggregates can be better represented.

4. Conclusions

The dependence of ice particle mass–dimensional relationships on median mass diameter (D_{mm}) is illustrated using Finlon et al.'s [13] technique for characterizing (a, b) mass–dimensional (m–D) coefficients as surfaces of equally plausible solutions. Using in situ observations of PSDs and coincident radar reflectivity (Z) observations at 13 GHz collected during OLYMPEX, surfaces of equally plausible (a, b) coefficients were derived by minimizing the chi-square difference between the observed Z and those computed from the PSDs. All solutions within a predefined threshold were deemed equally plausible. The 5928 5-s averaged data points with coincident radar and in situ measurements are sorted into 12 different populations using the median mass diameter defined using Heymsfield et al.'s [5] previously derived (a, b) coefficients ($D_{mm,hy}$) to explore this dependence.

A significant dependence of the m–D coefficients on $D_{mm,hy}$ was established for ice-phase clouds. Regardless of how the uncertainties from different sources are characterized and the choice of allowed tolerance, the same clockwise shift of the equally plausible surfaces with increasing $D_{mm,hy}$ is found, indicating a robust dependence of m–D coefficients on $D_{mm,hy}$. Statistics of 300 random equally plausible surfaces show significant negative correlation between $D_{mm,hy}$ and the mean values of both a and b solutions. The best estimates of (a, b) pairs that minimize the χ^2 for each population are

shown to be smaller than the HY04 coefficients and produce smaller effective densities when $D_{mm,hy} > 2500$ µm.

Periods with large $D_{mm,hy}$ between 3 and 6 mm are further discussed. The HY04 m–D relation generally accurately estimates Z for $D_{mm,hy} < 3$ mm, but increasingly overestimates Z for $D_{mm,hy}$ between 3 and 6 mm. Extensive large aggregates ranging in size with D between 3 and 5 mm and up to 1 cm were observed by the HVPS at temperatures −15–0 °C during OLYMPEX. Previous m–D relations designed for aggregates are also shown to produce less mass than HY04 m–D and those m–D relations derived for $D_{mm,hy} < 3$ mm in this study. The use of $D_{mm,hy}$-dependent m–D parameters improves agreement between the Z derived from PSDs and those bulk measurements.

Thus, the use of a constant m–D relationship is not able to explain particle mass when aggregates greater than 3 mm dominate. Multiple m–D relations are recommended to apply for different D_{mm} ranges. This could improve the retrievals of cloud bulk properties associated with hydrometer mass in remote sensing retrieval algorithms and numerical models. Future studies should further explore whether the same trends observed here also exist for clouds of different types and observed in different geographical locations and meteorological regimes, and assess to what extent the D_{mm}-dependent m–D relations improve the retrieval of cloud properties and the simulation of cloud processes.

References

1. Fontaine, E.; Leroy, D.; Schwarzenboeck, A.; Delanoë, J.; Protat, A.; Dezitter, F.; Grandin, A.; Strapp J. W.; Lilie, L.E. Radar reflectivity factors simulations of ice crystal populations from in situ observations for the retrieval of condensed water content in tropical mesoscale convective systems. *Atmos. Meas. Tech.* **2017**, *10*, 2239–2252. doi:10.5194/amt-10-2239-2017.

2. Mitchell, D.L.; Zhang, R.; Pitter, R.L. Mass-dimensional relationships for ice particles and the influence of riming on snowfall rates. *J. Appl. Meteorol.* **1990**, *29*, 153–163. doi:10.1175/1520-0450(1990)029<0153:MDRFIP>2.0.CO;2.

3. Heymsfield, A.J.; Matrosov, S.Y.; Wood, N.B. Toward improving ice water content and snow-rate retrievals from radars. Part I: X and W bands, emphasizing CloudSat. *J. Appl. Meteorol. Climatol.* **2016**, *55*, 2063–2090. doi:10.1175/JAMC-D-15-0290.1.

4. Brown, P.R.; Francis, P.N. Improved measurements of the ice water content in cirrus using a total-water probe. *J. Atmos. Ocean. Technol.* **1995**, *12*, 410–414. doi:10.1175/1520-0426(1995)012<0410:IMOTIW>2.0.CO;2.

5. Heymsfield, A.J.; Bansemer, A.; Schmitt, C.; Twohy, C.; Poellot, M.R. Effective ice particle densities derived from aircraft data. *J. Atmos. Sci.* **2004**, *61*, 982–1003. doi:10.1175/1520-0469(2004)061<0982:EIPDDF>2.0.CO;2.

6. Cotton, R.J.; Field, P.R.; Ulanowski, Z.; Kaye, P.H.; Hirst, E.; Greenaway, R.S.; Crawford, I.; Crosier, J.; Dorsey, J. The effective density of small ice particles obtained from in situ aircraft observations of mid-latitude cirrus. *Q. J. R. Meteorol. Soc.* **2013**, *139*, 1923–1934. doi:10.1002/qj.2058.

7. Westbrook, C.D.; Ball, R.C.; Field, P.R.; Heymsfield, A.J. Theory of growth by differential sedimentation, with application to snowflake formation, *Phys. Rev. E* **2004**, *70*, 021403. doi:10.1103/PhysRevE.70.021403.

8. Mace, S.B.; Benson, S.; Sonntag, K.L.; Kato, S.; Min, Q.; Minnis, P.; Twohy, C.H.; Poellot, M.; Dong, X.; Long, C.; et al. Cloud radiative forcing at the Atmospheric Radiation Measurement Program Climate Research Facility: 1. Technique, validation, and comparison to satellite-derived diagnostic quantities. *J. Geophys. Res*. **2006**, *111*, D11S90. doi:10.1029/2005JD005921.

9. Morrison, H.; Milbrandt, J.A. The altitude of snow growth by riming and vapor deposition in mixed-phase orographic clouds. *J. Atmos. Sci.* **2015**, *72*, 287–311. doi:10.1175/JAS-D-14-0065.1.

10. Lin, Y.; Colle, B.A. A new bulk microphysical scheme that includes riming intensity and temperature-dependent ice characteristics. *Mon. Weather Rev*. **2011**, *139*, 1013–1035. doi:10.1175/ 2010MWR3293.1.

11. Mitchell, D. Use of mass- and area-dimensional power laws for determining precipitation particle terminal velocities. *J. Atmos. Sci.* **1996**, *53*, 1710–1723. doi:10.1175/1520-0469(1996)053<1710:UOMAAD>2.0.CO;2.

12. Schmitt, C.G.; Heymsfield, A.J. On the occurrence of hollow bullet rosette– and column-shaped ice crystals in midlatitude cirrus. *J. Atmos. Sci.* **2007**, *64*, 4514–4519. doi:10.1175/2007JAS2317.1

13. Finlon, J.A.; McFarquhar, G.M.; Nesbitt, S.W.; Rauber, R.M.; Morrison, H.; Wu, W.; Zhang, P. A novel approach to characterize the variability in mass–dimension relationships: Results from MC3E. *Atmos. Chem. Phys.* **2019**, *19*, 3621–3643. doi:10.5194/acp-19-3621-2019.

14. Baran, A.J.; Bodas-Salcedo, A.; Cotton, R.; Lee, C. Simulating the equivalent radar reflectivity of cirrus at 94 GHz using an ensemble model of cirrus ice crystals: A test of the met office global numerical weather prediction model. *Q. J. R. Meteorol. Soc.* **2011**, *137*, 1547–1560. doi:10.1002/qj.870.

15. Heymsfield, A.J.; Bansemer, A.; Twohy, C.H. Refinements to ice particle mass dimensional and terminal velocity relationships for ice clouds: Part I: Temperature dependence. *J. Atmos. Sci.* **2007**, *64*, 1047–1067. doi:10.1175/JAS3890.1.

16. Heymsfield, A.J.; Schmitt, C.; Bansemer, A.; Twohy, C.H. Improved representation of ice particle masses based on observations in natural clouds. *J. Atmos. Sci.* **2010**, *67*, 3303–3318. doi:10.1175/2010JAS3507.1.

17. Abel, S.J.; Cotton, R.J.; Barrett, P.A.; Vance, A.K. A Comparison of ice water content measurement techniques on the FAAM Bae-146 aircraft. *Atmos. Meas. Tech*. **2014**, *7*, 3007–3022. doi:10.5194/amt-7-3007-2014.

18. McFarquhar, G.M.; Timlin, M.S.; Rauber, R.M.; Jewett, B.F.; Grim, J.A.; Jorgensen, D.P. Vertical variability of cloud hydrometeors in the stratiform region of mesoscale convective systems and bow echoes. *Mon. Weather Rev*. **2007**, *135*, 3405–3428. doi:10.1175/MWR3444.1.

19. Fontaine, E.; Schwarzenboeck, A.; Delanoë, J.; Wobrock, W.; Leroy, D.; Dupuy, R.; Gourbeyre, C.; Protat, A. Constraining mass–diameter relations from hydrometeor images and cloud radar reflectivities in tropical continental and oceanic convective anvils. *Atmos. Chem. Phys*. **2014**, *14*, 11367–11392. doi:10.5194/acp-14-11367-2014.

20. Kobayashi, R. Modeling and numerical simulations of dendritic crystal growth. *Physica D* **1992**, *63*, 410–423. doi:10.1016/0167-2789(93)90120-P.

21. Bailey, M.; Hallett, J. Growth rates and habits of ice crystals between −20 ° and −70 °C. *J. Atmos. Sci.* **2004**, *61*, 514–544. doi:10.1175/1520-0469(2004)061<0514:GRAHOI>2.0.CO;2.

22. Bailey, M.; Hallett, J. A comprehensive habit diagram for atmospheric ice crystals: Confirmation from the laboratory, AIRS II, and other field studies. *J. Atmos. Sci.* **2009**, *66*, 2888–2899. doi:10.1175/2009JAS2883.1.

23. Um, J.; McFarquhar, G.M.; Hong, Y.P.; Lee, S.S.; Jung, C.H.; Lawson, R.P.; Mo, Q. Dimensions and aspect ratios of natural ice crystals. *Atmos. Chem. Phys*. **2015**, *15*, 3933–3956. doi:10.5194/acp-15-3933-2015.

24. Locatelli, J.D.; Hobbs, P.V. Fall speeds and masses of solid precipitation particles. *J. Geophys. Res.* **1974**, *79*, 2185–2197. doi:10.1029/JC079i015p02185.

25. Holroyd, E.W. Some techniques and uses of 2D-C habit classification software for snow particles. *J. Atmos. Oceanic Technol.* **1987**, *4*, 498–511. doi:10.1175/1520-0426(1987)004<0498:STAUOC>2.0.CO;2.

26. McFarquhar, G.M.; Heymsfield, A.J.; Macke, A.; Iaquinta, J.; Aulenbach, S.M. Use of observed ice crystal sizes and shapes to calculate mean-scattering properties and multispectral radiances: CEPEX April 4, 1993, Case Study. *J. Geophys. Res*. **1999**, *104*, 31763–31779. doi:10.1029/1999JD900802.

27. Um, J.; McFarquhar, G.M. Single-scattering properties of aggregates of bullet rosettes in cirrus single-scattering properties of aggregates of bullet rosettes in cirrus. *J. Appl. Meteor. Climatol*. **2007**, *46*, 757–775. doi:10.1175/JAM2501.1.

28. Um, J.; McFarquhar, G.M. Single-scattering properties of aggregates of plates. *Q. J. R. Meteorol. Soc*. **2009**, *135*, 291–304. doi:10.1002/qj.378.

29. Lindqvist, H.; Muinonen, K.; Nousiainen, T.; Um, J.; McFarquhar, G.M.; Haapanala, P.; Makkonen, R.; Hakkarainen, H. Ice-cloud particle habit classification using principal components. *J. Geophys. Res. Atmos.* **2012**, *117*, 1–12. doi:10.1029/2012JD017573.

30. Praz, C.; Ding, S.; McFarquhar, G.M.; Berne, A. A versatile method for ice particle habit classification using airborne imaging probe data. *J. Geophys. Res. Atmos*. **2018**, *123*, 13472–13495. doi:10.1029/2018JD029163.

31. Touloupas, G.; Annika Lauber, A.; Jan Henneberger, J.; Alexander Beck, A.; Lucchi, A. A convolutional neural network for classifying cloud particles recorded by imaging probes. *Atmos. Meas. Tech.* **2020**, 13, 2219–2239.

32. Jackson, R.C.; McFarquhar, G.M.; Korolev, A.V.; Earle, M.E.; Liu, P.S.; Lawson, R.P.; Brooks, S.; Wolde, M.; Laskin, A.; Freer, M. The dependence of ice microphysics on aerosol concentration in arctic mixed-phase stratus clouds during ISDAC and M-PACE. *J. Geophys. Res. Atmos*. **2012**, *117*, 1–20. doi:10.1029/2012JD017668.

33. Finlon, J.A.; McFarquhar, G.M.; Rauber, R.M.; Plummer, D.M.; Jewett, B.F.; Leon, D.; Knupp, K.R. A comparison of X-band polarization parameters with in situ microphysical measurements in the comma head of two winter cyclones. *J. Appl. Meteor. Climatol*. **2016**, *55*, 2549–2574. doi:10.1175/JAMC-D-16-0059.1.

34. Erfani, E.; Mitchell, D.L. Developing and bounding ice particle mass- and area-dimension expressions for use in atmospheric models and remote sensing. *Atmos. Chem. Phys.* **2016**, *16*, 4379–4400. doi:10.5194/acp-16-4379-2016.

35. Khvorostyanov, V.I.; Curry, J.A. Terminal velocities of droplets and crystals: power laws with continuous parameters over the size spectrum. *J. Atmos. Sci.* **2002**, *59*, 1872–1884. doi:10.1175/1520-0469(2002)059<1872:TVODAC>2.0.CO;2.

36. Houze, R.A.; McMurdie, L.A.; Petersen, W.A.; Schwaller, M.R.; Baccus, W.; Lundquist, J.D.; Mass, C.F.; Nijssen, B.; Rutledge, S.A.; Hudak, D.R.; et al. The Olympic Mountains Experiment (OLYMPEX). *Bull. Am. Meteorol. Soc.* **2017**, *98*, 2167–2188. doi:10.1175/BAMS-D-16-0182.1.

37. Delene, D.; Hibert, K.; Poellot, M.; Brackin, N. The North Dakota Citation Research Aircraft Measurement Platform. *SAE Tech. Pap.* **2019**, doi:10.4271/2019-01-1990.

38. Field, P.R.; Wood, R.; Brown, P.R.A.; Kaye, P.H.; Hirst, E.; Greenaway, R.; Smith, J.A. Ice particle interarrival times measured with a fast FSSP. *J. Atmos. Ocean. Technol.* **2003**, *20*, 249–261. doi:10.1175/1520-0426(2003)020%3C0249:IPITMW% 3E2.0.CO;2.

39. Jackson, R.C.; McFarquhar, G.M.; Stith, J.; Beals, M.; Shaw, R.A.; Jensen, J.; Jensen, J.; Fugal, J.; Korolev, A. An assessment of the impact of antishattering tips and artifact removal techniques on cloud ice size distributions measured by the 2D cloud probe. *J. Atmos. Ocean. Technol.* **2014**, *31*, 2567–2590. doi:10.1175/JTECH-D-13-00239.1.

40. Heymsfield, A.J.; Parrish, J.L. A computational technique for increasing the effective sampling volume of the PMS two-dimensional particle size spectrometer. *J. Appl. Meteorol.* **1978**, *17*, 1566–1572. doi:10.1175/1520-0450(1978)017<1566:ACTFIT>2.0.CO;2.

41. Sadowy, G.; Berkun, A.C.; Chun, W.; Im, E.; Durden S. Development of an advanced airborne precipitation radar. *Microw. J.* **2003**, *46*, 84–98.

42. Durden, S.L.; Tanelli, S.; Sy, O.O. Comparison of GPM DPR and airborne radar observations in OLYMPEX. *IEEE Geosci. Remote Sens. Lett.* **2019**, doi:10.1109/LGRS.2019.2952287.

43. Chase, R.J.; Finlon, J.A.; Borque, P.; McFarquhar, G.M.; Nesbitt, S.W.; Tanelli, S.; Sy, O.O.; Durden, S.L.; Poellot, M.R. Evaluation of triple-frequency radar retrieval of snowfall properties using coincident airborne in situ observations during OLYMPEX. *Geophys. Res. Lett.* **2018**, *45*, 5752–5760. doi:10.1029/2018GL077997.

44. Lance, S.; Brock, C.A.; Rogers, D.; Gordon, J.A. Water droplet calibration of the Cloud Droplet Probe (CDP) and in-flight performance in liquid, ice and mixed-phase clouds during ARCPAC. *Atmos. Meas. Tech*. **2010**, *3*, 1683–1706. doi:10.5194/ amt-3-1683-2010.

45. Heymsfield, A.J.; Field, P.R.; Bailey, M.; Rogers, D.; Stith, J.; Twohy, C.; Wang, Z.; Haimov, S. Ice in clouds experiment-layer clouds. Part I: Ice growth rates derived from lenticular wave cloud penetrations. *J. Atmos. Sci.* **2011**, *68*, 2628–2654. doi: 10.1175/JAS-D-11-025.1.

46. Hogan, R.J.; Tian, L.; Brown, P.R.; Westbrook, C.D.; Heymsfield, A.J.; Eastment, J.D. Radar scattering from ice aggregates using the horizontally aligned oblate spheroid approximation. *J. Appl. Meteorol. Climatol.* **2012**, *51*, 655–671. doi:10.1175/JAMC-D-11-074.1.

47. Leroy, D.; Fontaine, E.; Schwarzenboeck, A.; Strapp, J.W. Ice Crystal Sizes in High Ice Water Content Clouds. Part I: On the Computation of Median Mass Diameter from in Situ Measurements. *J. Atmos. Ocean. Tech.* **2016**, *33*, 2461–76. doi:10.1175/JTECH-D-15-0151.1.

48. Heymsfield, A.; Bansemer, A.; Wood, N.B.; Liu, G.; Tanelli, S.; Sy, O.O.; Poellot, M.; Liu, C. Toward improving ice water content and snow-rate retrievals from radars. Part II: Results from three wavelength radar–collocated in situ measurements and CloudSat–GPM–TRMM radar data. *J. Appl. Meteorol. Climatol.* **2018**, *57*, 365–389. doi:10.1175/JAMC-D-17-0164.1.

49. van de Hulst, H.C. *Light Scattering by Small Particles*; John Wiley & Sons: New York, NY, USA, 1957.

50. Hogan, R.J.; Westbrook, C.D. Equation for the microwave backscatter cross-section of aggregate snowflakes using the self-similar Rayleigh–Gans approximation. *J. Atmos. Sci.* **2014**, *71*, 3292–3301. doi:10.1175/JAS-D-13-0347.1.

51. Tyynelä, J.; Leinonen, J.; Westbrook, C.; Moisseev, D.; Nousiainen, T. Applicability of the Rayleigh–Gans approximation for scattering by snowflakes at microwave frequencies in vertical incidence. *J. Geophys. Res.* **2013**, *118*, 1826−1839. doi:org/10.1002/jgrd.50167.

52. Leinonen, J.; Kneifel, S.; Hogan, R.J. Evaluation of the Rayleigh–Gans approximation for microwave scattering by rimed snowflakes. *Q. J. R. Meteorol. Soc.* **2018**, *144* (Suppl. S1), 77–88. doi:10.1002/qj.3093.

53. McFarquhar, G.M.; Um, J.; Freer, M.; Baumgardner, D.; Kok, G.L.; Mace, G. Importance of small ice crystals to cirrus properties: Observations from the tropical warm pool international cloud experiment (TWP-ICE). *Geophys. Res. Lett.* **2007**, *34*, 1–6. doi:10.1029/2007GL029865.

54. Korolev, A.; Strapp, J.W.; Isaac, G.A.; Emery, E. Improved Airborne Hot-Wire Measurements of Ice Water Content in Clouds. *J. Atmos. Ocean. Technol.* **2013**, *30*, 2121–2131. doi:10.1175/JTECH-D-13-00007.1.

55. Cober, S.G.; Isaac, G.A.; Korolev, A.V.; Strapp, J.W. Assessing cloud-phase conditions. *J. Appl. Meteorol.* **2001**, *40*, 1967–1983. doi:10.1175/1520-0450(2001)040<1967:ACPC>2.0.CO;2.

56. McFarquhar, G.M.; Hsieh, T.; Freer, M.; Mascio, J.; Jewett, B.F. The characterization of ice hydrometeor gamma size distributions as volumes in N0–λ–μ phase space: Implications for Microphysical Process Modeling. *J. Atmos. Sci.* **2015**, *72*, 892–909. doi:10.1175/JAS-D-14-0011.1.

57. Hallett, J. Measurement in the Atmosphere. In *Handbook of Weather, Climate, and Water*; Potter, T.D., Colman, B.R., Eds.; Wiley-Interscience: Hoboken, NJ, USA, 2005; pp. 711–720. doi:10.1002/0471721603.ch35.

58. Heymsfield, A.J.; Schmitt, C.; Bansemer, A. Ice Cloud Particle Size Distributions and Pressure-Dependent Terminal Velocities from In Situ Observations at Temperatures from 0 ° to −86 °C. *J. Atmos. Sci.*, **2013**, *70*, 4123–4154. doi:10.1175/JAS- D-12-0124.1.

59. Flatau, P.J.; Draine, B.T. Discrete-dipole approximation for scattering calculations. *J. Opt. Soc. Am. A* **1994**, *11*, 1491–1499. doi:10.1364/JOSAA.11.001491.

60. Tyynelä, J.; Leinonen, J.; Moisseev, D.; Nousiainen, T. Radar Backscattering from Snowflakes: Comparison of Fractal, Aggregate, and Soft Spheroid Models. *J. Atmos. Ocean. Technol.* **2011**, *28*, 1365–1372. doi:10.1175/JTECH-D-11-00004.1

61. Leinonen, J.; Szyrmer, W. Radar signatures of snowflake riming: A modeling study. *Earth Space Sci.* **2015**, *2*, 346–358. doi:10.1002/2015EA000102

62. Leroy, D.; Fontaine, E.; Schwarzenboeck, A.; Strapp, J.W.; Korolev, A.; McFarquhar, G.; Dupuy, R.; et al. Ice Crystal Sizes in High Ice Water Content Clouds. Part II: Statistics of Mass Diameter Percentiles in Tropical Convection Observed during the HAIC/HIWC Project. *J. Atmos. Ocean. Technol.* **2017**, *34*, 117–136. doi:10.1175/JTECH-D-15-0246.1

63. Schmitt, C.G.; Heymsfield, A.J. The dimensional characteristics of ice crystal aggregates from fractal geometry. *J. Atmos. Sci.* **2010**, *67*, 1605–1616.